

Phononics of Graphene Interfaced with Flowing Ionic Fluid: An Avenue for High Spatial Resolution Flow Sensor Applications

Alireza Ahmadian Yazdi, Jie Xu, and Vikas Berry*



Cite This: *ACS Nano* 2021, 15, 6998–7005



Read Online

ACCESS |



Metrics & More



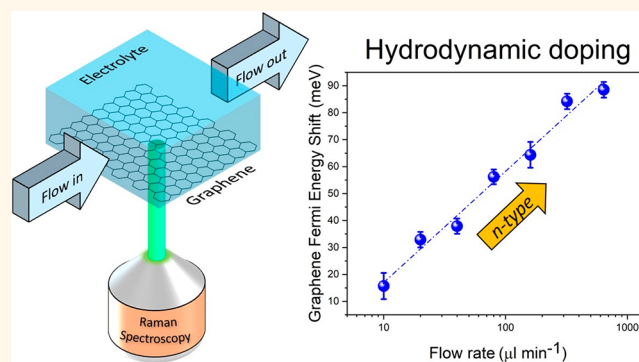
Article Recommendations



Supporting Information

ABSTRACT: While ionic flow over graphenic structures creates electromotive potential, there is a need to understand the local carrier density induced in graphene without any electrode-induced Fermi-level pinning. Here, we show the electrolyte-flow induced localized doping in graphene *via* inspecting its Raman phononic energy. Graphene's Fermi energy level has a logarithmic dependence to the flow velocity over 2 orders of magnitude of velocity ($\sim 100 \mu\text{m s}^{-1}$ to 10 mm s^{-1}). A theoretical model of the electric double layer (EDL) during ionic transport is used to correlate the Fermi level of graphene with the flow rate and the electronic structure (HOMO-LUMO levels) of the ionic species. This correlation can allow us to use graphene as a reliable, non-invasive, optical flow-sensor, where the flow rates can be measured at high spatial resolution for several lab-on-a-chip applications.

KEYWORDS: graphene, Raman spectroscopy, nanosensor, flow sensor, electric double layer



The intriguing interaction of low-dimensional carbon materials with a flowing liquid has been the subject of many studies since more than a decade ago. Ghosh *et al.*¹ were the first to observe and measure an induced voltage on carbon nanotubes (CNTs) due to contact with a flowing liquid. This phenomenon was attributed to the fluctuating Coulombic fields of the liquid which, in turn, impose a flow of charge carriers in CNT. On this basis, the first CNT flow sensor was born, and soon after, it initiated a stream of similar experiments on CNTs,^{2–7} and later on graphene^{8–10} with applications that went beyond sensing flow rate, and aimed at harvesting electricity from a liquid flow.¹¹ Despite major advancements, several questions about the mechanism underlying this phenomenon, referred to as “hydrovoltaics”, remain unaddressed. For example, the change in flow-induced voltage with flow rate was found to be linear^{5,9,10,12} in some studies and strongly nonlinear (nearly logarithmic)^{1,3,7,8,13} in others. This led to a wide variety of models capable of explaining specific experimental data including streaming potential,⁵ phonon drag,¹² fluctuating asymmetric potential,¹ and surface ion hopping.⁷ Although the existing disagreements are part of the complex nature of graphene-flow interaction, there needs to be an effort to produce a more unified explanation that fits a broader range of experimental results. Such efforts would eventually help us to unlock the full potential of hydrovoltaic

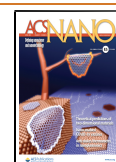
technologies, including relevant sensors, and energy harvesting devices.

Previous experimental studies on fluid flow interaction with graphene and CNTs have relied on measuring the voltage drop across or along the flow direction and correlating it to the flow velocity. However, the influence of the metal electrodes connected to the graphene or CNTs is unclear. In fact, there is experimental evidence that, once these electrodes are isolated from interacting with the flow, flow-induced voltage disappeared,⁸ suggesting that electrolyte polarization on the metal electrodes may have been the source for the observed voltage. This suggests that alternative methods capable of directly screening the flow-graphene interaction should be sought. Since the emergence of graphene, Raman spectroscopy has been used extensively as a fast, nondestructive, and high resolution tool for studying its charged carrier properties.^{14–16} This is partly due the large electron-phonon coupling,

Received: January 2, 2021

Accepted: April 7, 2021

Published: April 9, 2021



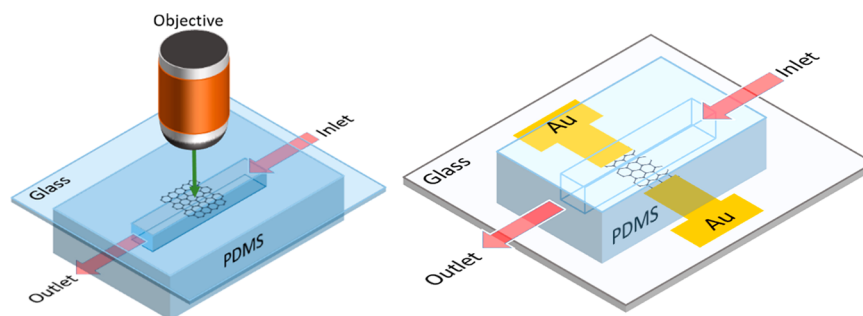


Figure 1. (Left) Schematic of the optical graphene flow analyzer. (Right) Schematic of the graphene FET devices for electrical measurements. The microchannel is placed carefully to ensure the Cr/Au contacts are covered with PDMS; therefore, only the graphene channel is exposed to the solution. Note that microfluidic fittings for inlet and outlet flows are not shown in these images.

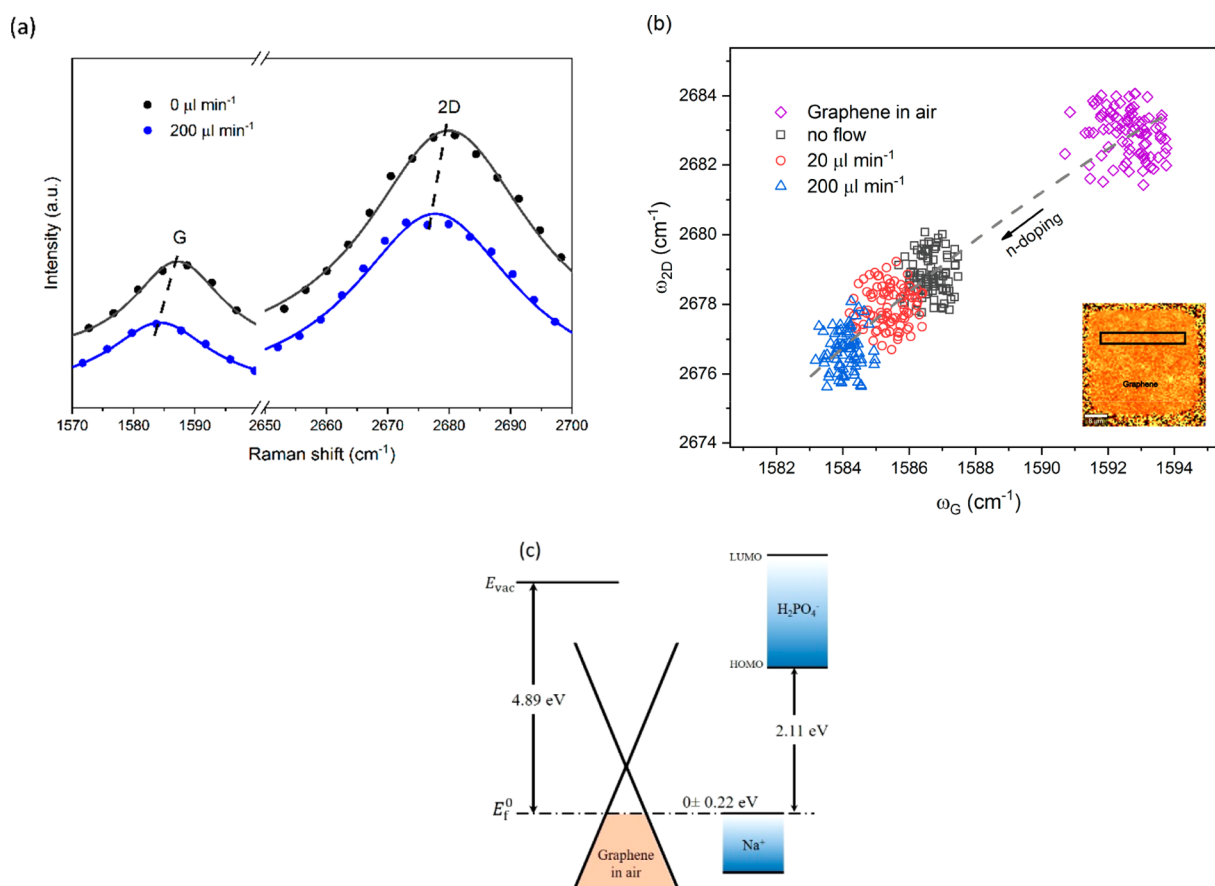


Figure 2. (a) Raman spectra of graphene in the presence of sodium hydrogen phosphate solution (0.2 M Na_2HPO_4). The dotted lines qualitatively illustrate the trends for the shifts observed in G and 2D peaks. The spectra are fitted with a Lorentz function. (b) G peak position ω_G (cm^{-1}) with respect to 2D peak position ω_{2D} (cm^{-1}) obtained for several points within the solid rectangle in the subset image. The dashed line shows the theoretical trend for n-doping.^{19,21} The subset image demonstrates the Raman mapping of the graphene square piece for 2D peak position with the scale bar being 8 μm in size. (c) Schematic diagram for the energy level of the ionic species at the graphene/solution interface. E_f^0 refers to the Fermi energy with respect to that of the vacuum level which for graphene is assumed to be 4.57 eV in the undoped state.²⁷ This value is then shifted to 4.89 eV due to the initial *p*-type doping (~ 317 meV calculated from the Raman measurements). HOMO and LUMO levels for Na^+ are for those ions within 0.1–0.4 nm distance from the graphene/liquid interface.²³ The energy levels for H_2PO_4^- were estimated from the data in ref 28.

rendering graphene's Raman peaks (frequency, width, and height) to respond sensitively to any variation of its electronic properties.¹⁷ The very sensitive Raman peaks combined with the outstanding large surface area allow us to use graphene's Raman spectroscopy as a reliable tool for studying various interfacial phenomena.^{18–20} As to the study of graphene-flow interaction, Raman spectroscopy eliminates possible interference caused by externally applied electric or magnetic fields

that exists in other methods of probing hydrovoltaics, such as field-effect transistors and Hall-bar measurements. In the present study, we employed a Raman spectroscopy approach to observe the extent to which a flow of an electrolyte inside a microchannel induces doping in graphene. Once the flow-induced doping is established, we then characterized the system sensitivity and showed that the graphene's Fermi energy level has a strong logarithmic dependence to the flow

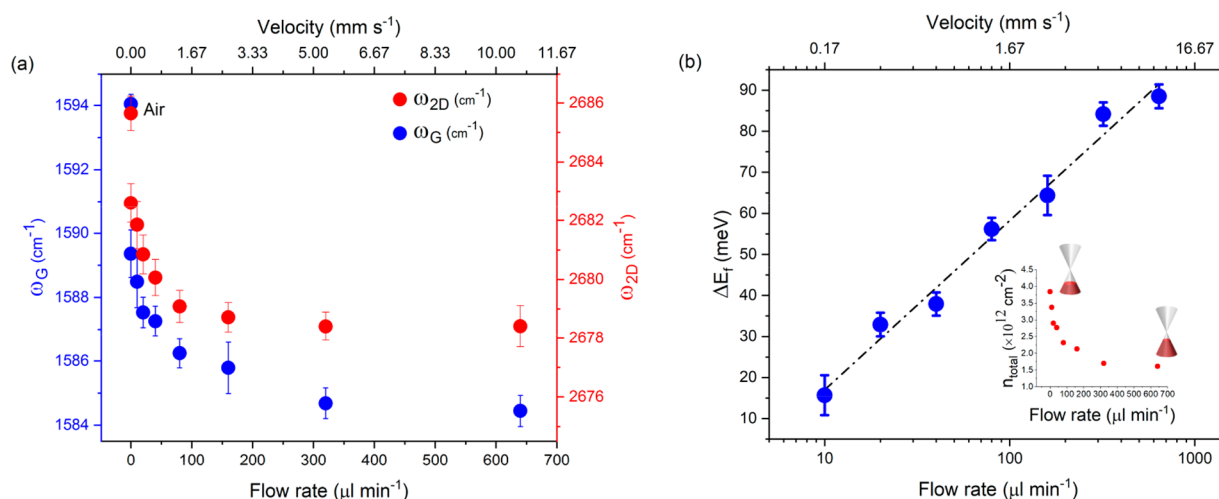


Figure 3. (a) ω_{2D} and ω_G with respect to flow rate, and the corresponding average velocity on the top axis calculated by dividing the flow rate with the cross-sectional area of 1 mm^2 . The error bar at each data point corresponds to the standard deviation calculated from averaging 50 spectra. (b) Flow-induced Fermi energy shift ΔE_f with respect to static liquid. The dashed line shows the linear fit with a slope of 41.24, and R-squared value of 0.98. The error bars originate from the standard mean error of calculating G peaks during the measurement. The inset shows the nearly logarithmic decay of total carrier concentration n_{total} with positive polarity with respect to flow rate, with the schematic of the occupied states being shown for the two ends of the graph. The electrolyte is an aqueous solution of $0.2 \text{ M Na}_2\text{HPO}_4$.

velocity over two decades of velocity ($\sim 100 \mu\text{m s}^{-1}$ to 10 mm s^{-1}). To provide a theoretical picture of the flow-induced doping effect, we first compared our optical measurements to a conventional electrical measurement of hydrovoltaics in a similar experimental setup. At last, through a numerical simulation of Nernst–Planck equations, we showed that flow-induced doping in graphene can be explained by a continuum model of charge transport within the electric double layer (EDL) under a viscous flow.

RESULT AND DISCUSSION

The Raman spectrum of monolayer graphene is characterized by two prominent G (*ca.* 1580 cm^{-1}) and 2D (*ca.* 2700 cm^{-1}) peak positions, and a disorder-induced D peak position (*ca.* 1350 cm^{-1}), each corresponding to a specific phononic vibrational mode.¹⁴ Because of a large electron-phonon coupling strength in graphene, the position of these peaks is sensitive to any change that impacts graphene's electronic and physical structure.^{14–16} For instance, when graphene is negatively (positively) doped either electrically (*e.g.*, gate voltage) or chemically (*e.g.*, chemical functionalization), the 2D peak shifts to a lower (higher) frequency, whereas the G peak always shifts to a higher frequency with respect to undoped graphene.^{14,19,21,22} We leveraged this fundamental concept to design two sets of experiments that would establish the working principle of a graphene optical flow sensor: (i) We examined Raman spectroscopy of graphene in contact with the electrolyte flow to verify the flow-induced doping in graphene. (ii) To shed light on the mechanisms that cause flow-induced doping, we performed optical and electrical measurements, and compared these findings to our numerical simulation results.

Figure 1(left) demonstrates the typical experimental setup for optical measurements. In our device, graphene is located relatively in the middle of the microchannel to avoid hydrodynamic entrance region effects. In the first set of experiments, we injected an ionic solution of 0.2 M sodium hydrogen phosphate (Na_2HPO_4) into the microchannel with a syringe pump. We then performed spatial Raman scan over the entire graphene sheet ($40 \times 40 \mu\text{m}^2$) at different flow rates (0,

20, $200 \mu\text{L min}^{-1}$). The spot size of the laser is *ca.* $0.7 \mu\text{m}$ ($50\times$ objective at 532 nm wavelength); thus, we acquired 80×80 Raman spectra to ensure the entire sheet is scanned.

Figure 2a demonstrates the typical Raman spectra recorded for a single spot. Both 2D and G peaks shift to lower frequencies once the liquid flows at $200 \mu\text{L min}^{-1}$, verifying the sensitivity to flow rate. To extend these results, we acquired Raman spectra of several other points on the graphene sheet and plotted their G peak ω_G (cm^{-1}) with respect to their 2D peak frequencies ω_{2D} (cm^{-1}) (Figure 2b). The initial position of G and 2D peaks for the graphene in air (purple points) and the red shift in both G and 2D peaks after the electrolyte comes into contact with the graphene imply that the initial doping in graphene is *p-type*.²¹ This is attributed to the CVD synthesis and acid-containing transfer of graphene onto the glass slides. Second, the location of black points compared to purple points in Figure 2b implies that the electrolyte at rest imposes a large n-doping, represented by the simultaneous red shift of both G and 2D peaks by nearly 6 units. An aqueous solution of Na_2HPO_4 contains sodium Na^+ and dihydrogen phosphate H_2PO_4^- ions. Comparing the energy levels of these ionic species with the graphene Fermi level E_f^0 (calculated with respect to vacuum) in Figure 2c, it may be inferred that H_2PO_4^- has a high tendency to n-dope graphene by transferring electrons, whereas the doping effect of alkali cations Na^+ is much weaker, and its polarity depends on the distance from the interface.²³ Therefore, adsorption of H_2PO_4^- ions may have contributed significantly to the large n-doping observed for no flow case in Figure 2b. It is also noteworthy that Na^+ ions may contribute to this overall n-doping *via* specific mechanisms, such as intercalation between graphene and glass through holes and defects,²⁴ as well as bonding to oxygen functionalities on the graphene surface.²⁵ Now we turn our attention to the impact of the electrolyte flow on the graphene doping level. As seen in the red points in Figure 2b, once the liquid begins to flow at $20 \mu\text{L min}^{-1}$, graphene becomes even more n-doped which continues to enhance at $200 \mu\text{L min}^{-1}$. This suggests that the hydrodynamics of the flow alone is capable of inducing a net doping shift (here n-

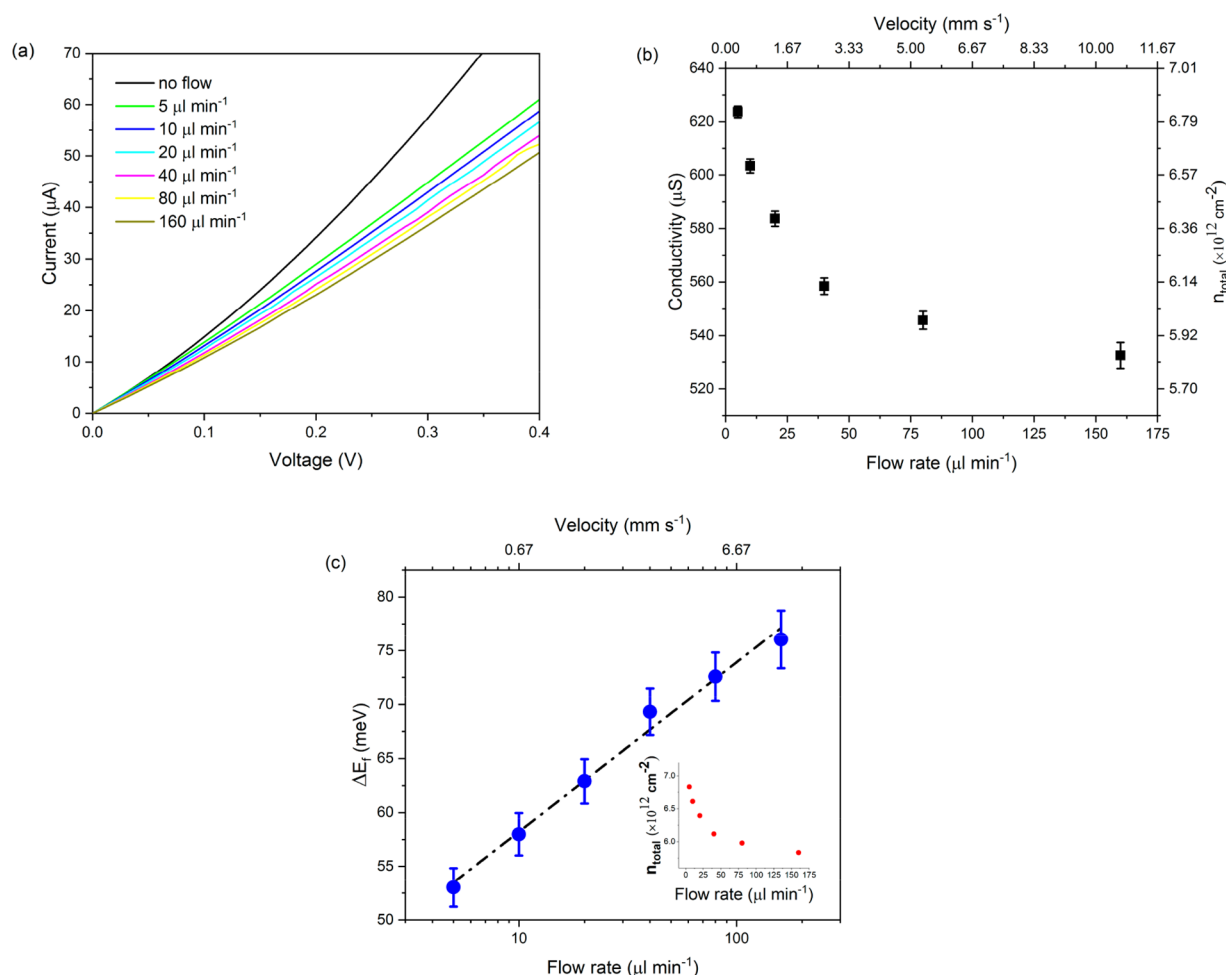


Figure 4. (a) I – V curves of electrolyte-gated graphene at different flow rates. (b) Conductivity of the graphene channel versus flow rate. The top axis demonstrates the average velocity corresponding to the microchannel of 0.25 mm^2 cross-sectional area. (c) Fermi energy change ΔE_f with respect to the static liquid at different flow rates. The dashed line shows the linear fit with a slope of 7.94, and R -squared value of 0.98. The subset graph plots total carrier concentration n_{total} at different flow rates. All the error bars originate from the linear fitting errors of the I – V curves in image (a).

doping) in graphene, which has not been reported prior to this study. More interestingly, each scan spot (*ca.* $0.7 \mu\text{m}$ in size at $50\times$ objective) corresponding to individual points in Figure 2b can be regarded as a nanoscale indicator of the flow rate.

In the past, electrical measurement tools such as FETs were able to provide evidence of flow-induced voltage generation, namely, hydrovoltaics, in low-dimensional carbon materials such as graphene and CNTs. Thus, several FET-based flow sensors and electricity harvesting devices were proposed.^{1,3,9,10,13,26} However, the optical flow sensor introduced here offers several advantages over conventional FET-based devices. First, in practice, such an optical flow sensor eliminates the need for complex and costly fabrication of FETs, and the laborious task of integrating them into a microfluidic device. As to the application, Raman spectroscopy enables remote measurement of flow rate suitable when handling liquids containing sensitive or hazardous chemicals and biochemical reagents or entities. Moreover, Raman spectroscopy is an optical measurement tool; hence, it experiences less signal interference compared to FETs or electrochemical measurements. A notable example that verifies this notion is the study performed by Yin *et al.*⁸ in which the flow-induced voltage in graphene FETs was attributed mostly to the solution

polarization at the electrode/solution rather than graphene/solution interface.

Figure 3 characterizes a hydrodynamically doped graphene sheet and quantifies the performance of the resulting optical flow sensor. To obtain the graph in Figure 3a, at each flow rate, we recorded the time-averaged Raman spectrum (50 spectra with 1 s intervals) for a single spot size *ca.* $1.5 \mu\text{m}$ ($20\times$ objective). This temporal measurement is important, as it reduces to a large extent the unsteady fluctuations, and possible hysteresis effects in Raman spectroscopy.²¹ The acquired spectra were then fitted with a Lorentz function to obtain ω_{2D} and ω_G . From the data in Figure 3a, we calculated the Fermi energy level E_f (meV) and total carrier concentration n_{total} (cm^{-2}) to quantify flow-induced doping in graphene. Briefly, for p-doped graphene, E_f (meV) = $-18\Delta\omega - 83$, in which $\Delta\omega$ (cm^{-1}) is the G peak frequency shift with respect to undoped graphene ($\sim 1580 \text{ cm}^{-1}$).²² Next, total carrier concentration n_{total} (cm^{-2}) was found using the relation: E_f (meV) = $\pm 1.283 \times 10^{-4} \sqrt{n_{\text{total}}}$, where the positive (negative) sign refers to n-doping (p-doping).²¹ Figure 3b plots the flow-induced change in Fermi energy ΔE_f calculated by subtracting the E_f value at zero flow rate from E_f values at non-zero flow rates, *i.e.*, $\Delta E_f = E_{f,\text{flow}} - E_{f,\text{static}}$. As seen, ΔE_f increases

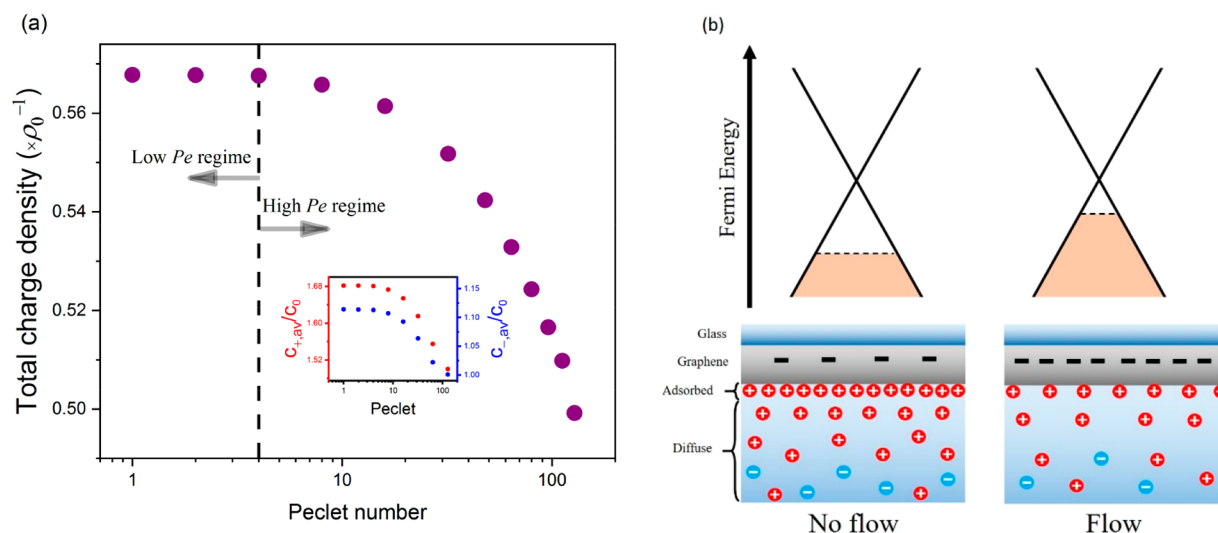


Figure 5. (a) Dimensionless total charge density in graphene's EDL with respect to the flow Peclet number. ρ_0 is a reference charge calculated as eZc_0 . The subset plot demonstrates the EDL-averaged concentration of \pm ionic species with respect to the Peclet number. (b) Variation of EDL charge, charge carrier concentration in graphene, and the corresponding Fermi energy level before and after the electrolyte flow.

logarithmically with increasing the flow rate, indicating that $\Delta E_f \propto \log(\alpha u)$, with u being the average flow velocity, and α being a constant. The increase in ΔE_f can be explained by the sublinear decay (nearly logarithmic) of the total carrier concentration (n_{total}) with positive polarity, shown in the subset of Figure 3b. The data in Figure 3 reveal two prominent features of flow-induced doping in graphene: (i) ω_{2D} , ω_G , and n_{total} demonstrate a strong sublinear relation (almost logarithmic) to flow rate with a saturation at high flow rates. (ii) The Fermi energy shift corresponding to flow-induced doping has an excellent logarithmic dependence to flow rate.

In order to investigate the impact of the electrolyte properties on the observed hydrodynamic doping effect, we adjusted the pH of the Na_2HPO_4 solution by adding 0.2 M sodium dihydrogen phosphate NaH_2PO_4 (acidic) and repeated the above measurements. As seen in Figure S2, we still observe a hydrodynamic doping effect at both pH 8 and 5 solutions with a similar linear logarithmic trend to Figure 3, suggesting that hydrodynamics dominates the overall doping compared to the well-known pH-induced doping.¹⁹ It is also important to realize the impact of ionic strength in flow sensing applications.^{5,9} Thus, we repeated these measurements with 10 and 1 mM Na_2HPO_4 solutions that have an ionic strength of *ca.* 30 mM and *ca.* 3 mM, respectively, with relatively similar pH values (~ 9.2). As shown in Figure S3, at higher ionic strength, the nanosensor responds less sensitively to the change in flow rate as indicated by the slope of the linearized graph (in agreement with ref 9). This is due to the fact that, at larger ionic strength, the EDL is thinner according to the Debye screening length; thus, the majority of graphene charge carriers are effectively being screened by a compact layer of counterions at the interface, leading to a compromised sensitivity (Figure S3 subset).^{29–31}

The flow-induced shift in graphene Fermi energy measured in our optical experiments is in analogy with flow-induced voltage, or hydrovoltaics, in graphene and CNTs.^{1,3,13,26} This suggests that a similar underlying mechanism for both phenomena should exist regardless of the method of measurement. To examine this further, we repeated the flow

rate measurements with a graphene FET embedded inside a microchannel, as illustrated in Figure 1 (right). In order to prevent the impact that electrolyte polarization on Au electrodes might have on the results, these electrodes were carefully covered with PDMS to be isolated from any flow interaction. Figure 4a demonstrates the I – V response of the graphene channel gated by the electrolyte to the change in flow rate. From these data, we approximated the conductivity for the graphene channel with a length-to-width ratio of 4. Figure 4b plots the dependence of conductivity to the flow rate, with the total carrier concentration n_{total} being shown on the right axis. To calculate n_{total} , we used $\sigma = \mu n_{\text{total}}$, where μ is the carrier mobility in electrolyte-gated graphene calculated to be $569.7 \text{ cm}^2 \text{ V}^{-1} \text{ s}^{-1}$ (Supporting Information). Moreover, Figure 4c shows the variation of the corresponding Fermi energy level ΔE_f with respect to the electrolyte at rest, calculated using the method mentioned previously for the analysis in Figure 3b. Comparing Figure 4c and Figure 3b reveals similar features to which we alluded earlier; both experiments reveal that increasing the flow rate decreases n_{total} , and the ΔE_f has a strong logarithmic dependence to flow rate. As to the sensitivity, the comparison between the slope of the linearized graph in Figure 3b and Figure 4c (*ca.* 8 and 41, respectively) reveals that the FET device has less sensitivity to the change in flow rate. This can be attributed to the surface contaminations (*e.g.*, PMMA or copper residues) on graphene in the FET device, masking the interaction of its entire surface area with the surrounding liquid (Figure S1c).

The consistency between our findings in the optical and electrical experiments confirms that the observed hydrodynamic doping and hydrovoltaics originate from a similar mechanism. However, there are several contradicting models that have explained hydrovoltaics, and a unified theory explaining the phenomenon is needed. To put it into perspective, existing models have leveraged two approaches in regard to the scale of the theoretical analysis: (i) Molecular-scale approaches that lead to theories such as electron drag and stick-slip models.^{1–3,6,13,26} In essence, these models argue that the flow-induced electric current stems from a net slip motion

of an adsorbed layer of ions on graphene or CNTs, dragging the free charge carriers along the flow. While these effects cannot be ruled out due to the existing evidence,^{2,6,7} we can safely assume their contribution is negligible compared to the larger electrokinetic effects. This is due to the fact that the adsorbed ionic layer and water molecules only slip within nanometer distances on the graphene surface,³² thus only impacting local charge carriers. (ii) Continuum-scale approaches that lead to electric double layer (EDL) models and their subsequent electrokinetic effects, most importantly the streaming potential, have also been proposed.^{2,3,13,26} However, streaming potential, as used in previous studies, predicts a linear relation between variation of the local liquid potential (with respect to a reference) and flow rate; thus, it fails to explain the strong sublinear behavior observed in our electrical and optical experiments as well as in other studies.^{1,3,13} Despite this shortcoming, here we argue that the observed hydrodynamic doping is driven largely by the impact that the viscous flow might have on the EDL forming at the graphene/electrolyte interface. To verify this notion, we performed a numerical analysis of the EDL on a graphene's surface located in a slit microchannel (Figure S4). In this EDL, two identical ionic species with opposite charges distribute around the negatively charged surface of graphene on the glass slide. The concentration of these ions can be best expressed by the Nernst–Planck conservation equations written as³³

$$\frac{\partial c_{\pm}}{\partial t} = -\nabla \cdot (c_{\pm} \mathbf{u} - D_{\pm} \nabla c_{\pm} - c_{\pm} \mu_{\pm} \nabla \psi) \quad (1)$$

where \mathbf{u} represents the velocity field, D_{\pm} is the diffusivity, and μ_{\pm} is the ionic mobility term. Moreover, ψ denotes the potential distribution near the graphene's surface explained by the Poisson's equation

$$\nabla^2 \psi = -\frac{eZ(c_+ - c_-)}{\epsilon} \quad (2)$$

in which Z is the valence number of ions, and ϵ is the permittivity of the solvent. Equations 1 and 2, along with the Navier–Stokes equations, were solved numerically in dimensionless form to obtain ionic charge distribution c_{\pm} , and ψ in steady state condition. For a detailed numerical procedure, including assumptions, computational domain, and validation of our algorithm, we refer the reader to the [Supporting Information](#). Figure 5a demonstrates the dimensionless total charge density $[eZ(c_+ - c_-)/\rho_0]$, where ρ_0 is eZc_0 within graphene's EDL at different flow velocities represented by the Peclet number ($Pe = u_{PD}H/D$, where u_{PD} is the centerline velocity, H is the half-channel height, and D is the diffusion coefficient assumed to be similar for both \pm ions). This graph reveals two flow regimes: (i) The low Pe regime in which the total ionic charge is not impacted by the flow hydrodynamics. This is reasonable as the convective transport of ions is negligible at low flow velocities compared to the molecular diffusion and the electromigration in eq 1. (ii) The high Pe regime, where the convective transport takes effect, and gradually decreases the total ionic charge of the EDL with positive polarity (Figure 5a), as well as the average concentration of ions c_{\pm} (subset of Figure 5a). Since the electrons in graphene are constantly being screened by the positively charged ions c_+ near the graphene/electrolyte interface, the reduction in c_+ causes the graphene to become more n-doped. This is in agreement with our optical and

electrical measurements in which n_{total} decreases, and graphene becomes more n-doped by increasing the flow rate (Figure 2, and the subsets of Figure 3b and Figure 4c). More interestingly, the logarithmic decay of EDL charge at the high Pe regime in Figure 5a is analogous to the logarithmic decay of graphene's charge carriers demonstrated in Figure 3b and Figure 4b. This verifies that the carrier concentration in graphene is strongly influenced by ionic charge distribution. All this evidence collectively suggests that the hydrodynamic doping in graphene is essentially driven by the change in EDL charge due to the convective transport of ions near the interface. As to the sensing performance, Figure 5a also suggests that a possible flow sensor works only at a high Pe regime; thus, sensing extremely low flow rates requires further research, and it can be a subject of future studies.

CONCLUSION

In conclusion, we showed that the flow of an electrolyte induces a net doping in graphene, which can be monitored directly by Raman spectroscopy. On this basis, we introduced an optical graphene sensor capable of screening flow velocity in an outstanding range of $\sim 100 \mu\text{m s}^{-1}$ to 10 mm s^{-1} . The underlying mechanism leading to hydrodynamically doped graphene is the impact of flow velocity on ionic charge distribution within graphene's EDL. In fact, our numerical simulation showed that, at high Pe flows, the convective transport of ionic species near the interface reduces the net ionic charge, rendering a change in graphene doping and Fermi energy level. This model explains to a great extent our measurements in both the optical and the electrical experiments. It is noted that the use of suspended graphene may clarify the graphene/flow interaction in more detail by excluding the substrate-induced doping; however, the experimental setup to study this effect remain challenging. Overall, we envision that this graphene-based high-resolution optical flow-sensor would be a good fit for several lab-on-a-chip technologies. In fact, this non-invasive measurement of flow rate by Raman spectroscopy may find applications for liquids containing sensitive biological or chemical reagents.

METHODS

Fabrication of Phononic Flow Sensor. Single layer graphene was grown on copper foil via a chemical vapor deposition (CVD) method²⁰ and transferred onto a SiO₂/Si chip (300 nm SiO₂) for quality test and glass slides (0.13–0.17 mm thick, Corning) for microfluidic experiments. The graphene samples on glass slides were patterned into μm -scale shapes via photolithography and reactive ion etching (RIE, Trion Technology). These μm -scale sheets were able to sustain their attachment to the glass slides even at very high flow rates ($1000 \mu\text{L min}^{-1}$) as opposed to large graphene pieces of *ca.* 1 cm^2 area crumpled under such conditions. The graphene assembly was integrated into a microfluidic chamber built from polydimethylsiloxane (PDMS) using standard soft lithography techniques. The inbuilt microchannels were punched with holes for inlet and outlet of liquid and carefully bonded to glass slides containing graphene with super glue.

Fabrication of Graphene Field Effect Transistor (FET). The fabrication of the graphene FET was done using a wet etch method. At first, the Cr/Au (10/40 nm) layer was deposited on graphene transferred on glass slides using electron beam evaporation. The sample was then coated with AZ 1518 photoresist at 4000 rpm for 40 s, followed by patterning the contact pads with a mask aligner (Karl Suss MA6 Mask Aligner, 900 W UV power). The excess metal was etched away by dipping the sample in Au and Cr etching solutions. Finally, another round of similar photolithography was performed to

pattern the graphene into μm -scale rectangles acting as FET channels. Then, the excess graphene was etched away *via* reactive ion etching (RIE, Trion Technology). Two source meters (Keithley 2612) were used to characterize the FET device, and an Ag/AgCl electrode was used as the reference electrode when needed.

ASSOCIATED CONTENT

Supporting Information

The Supporting Information is available free of charge at <https://pubs.acs.org/doi/10.1021/acsnano.1c00020>.

Calculation of graphene's carrier mobility; AFM study of graphene samples; the impact of the background electrolyte; and numerical simulation details with the corresponding validation (PDF)

AUTHOR INFORMATION

Corresponding Author

Vikas Berry – Department of Chemical Engineering,
University of Illinois at Chicago, Chicago, Illinois 60607,
United States; orcid.org/0000-0002-1102-1996;
Email: vikasb@uic.edu

Authors

Alireza Ahmadian Yazdi – Department of Mechanical and
Industrial Engineering and Department of Chemical
Engineering, University of Illinois at Chicago, Chicago, Illinois
60607, United States

Jie Xu – Department of Mechanical and Industrial
Engineering, University of Illinois at Chicago, Chicago, Illinois
60607, United States

Complete contact information is available at:

<https://pubs.acs.org/doi/10.1021/acsnano.1c00020>

Notes

The authors declare no competing financial interest.

ACKNOWLEDGMENTS

The authors acknowledge the financial support from the Office of Naval Research (N00014-18-1-2583), National Science Foundation (Grants: CMMI-1503681 and CMMI-1030963), Early Career Faculty grant (80NSSC17K0522) from NASA's Space Technology Research Grants Program, and University of Illinois at Chicago.

REFERENCES

- (1) Ghosh, S.; Sood, A.; Kumar, N. Carbon Nanotube Flow Sensors. *Science* **2003**, 299 (5609), 1042–1044.
- (2) Xu, B.; Chen, X. Liquid Flow-Induced Energy Harvesting in Carbon Nanotubes: A Molecular Dynamics Study. *Phys. Chem. Chem. Phys.* **2013**, 15 (4), 1164–8.
- (3) Ghosh, S.; Sood, A.; Ramaswamy, S.; Kumar, N. Flow-Induced Voltage and Current Generation in Carbon Nanotubes. *Phys. Rev. B: Condens. Matter Mater. Phys.* **2004**, 70 (20), 205423.
- (4) Cohen, A. E. Carbon Nanotubes Provide a Charge. *Science* **2003**, 300, 1235–1236. DOI: [10.1126/science.300.5623.1235](https://doi.org/10.1126/science.300.5623.1235) (Author reply to: Carbon Nanotube Flow Sensors).
- (5) Bourlon, B.; Wong, J.; Miko, C.; Forro, L.; Bockrath, M. A Nanoscale Probe for Fluidic and Ionic Transport. *Nat. Nanotechnol.* **2007**, 2 (2), 104–7.
- (6) Kral, P.; Shapiro, M. Nanotube Electron Drag in Flowing Liquids. *Phys. Rev. Lett.* **2001**, 86 (1), 131–134.
- (7) Persson, B. N. J.; Tartaglino, U.; Tosatti, E.; Ueba, H. Electronic Friction and Liquid-Flow-Induced Voltage in Nanotubes. *Phys. Rev. B: Condens. Matter Mater. Phys.* **2004**, 69 (23), 235410.
- (8) Yin, J.; Zhang, Z.; Li, X.; Zhou, J.; Guo, W. Harvesting Energy from Water Flow over Graphene? *Nano Lett.* **2012**, 12 (3), 1736–41.
- (9) Newaz, A. K.; Markov, D. A.; Prasai, D.; Bolotin, K. I. Graphene Transistor as a Probe for Streaming Potential. *Nano Lett.* **2012**, 12 (6), 2931–5.
- (10) He, R. X.; Lin, P.; Liu, Z. K.; Zhu, H. W.; Zhao, X. Z.; Chan, H. L.; Yan, F. Solution-Gated Graphene Field Effect Transistors Integrated in Microfluidic Systems and Used for Flow Velocity Detection. *Nano Lett.* **2012**, 12 (3), 1404–9.
- (11) Zhang, Z.; Li, X.; Yin, J.; Xu, Y.; Fei, W.; Xue, M.; Wang, Q.; Zhou, J.; Guo, W. Emerging Hydrovoltaic Technology. *Nat. Nanotechnol.* **2018**, 13 (12), 1109–1119.
- (12) Kral, P.; Shapiro, M. Nanotube Electron Drag in Flowing Liquids. *Phys. Rev. Lett.* **2001**, 86 (1), 131.
- (13) Dhiman, P.; Yavari, F.; Mi, X.; Gullapalli, H.; Shi, Y.; Ajayan, P. M.; Koratkar, N. Harvesting Energy from Water Flow over Graphene. *Nano Lett.* **2011**, 11 (8), 3123–7.
- (14) Ferrari, A. C.; Basko, D. M. Raman Spectroscopy as a Versatile Tool for Studying the Properties of Graphene. *Nat. Nanotechnol.* **2013**, 8 (4), 235–46.
- (15) Malard, L. M.; Pimenta, M. A.; Dresselhaus, G.; Dresselhaus, M. S. Raman Spectroscopy in Graphene. *Phys. Rep.* **2009**, 473 (5–6), 51–87.
- (16) Ferrari, A. C.; Meyer, J. C.; Scardaci, V.; Casiraghi, C.; Lazzeri, M.; Mauri, F.; Piscanec, S.; Jiang, D.; Novoselov, K. S.; Roth, S.; Geim, A. K. Raman Spectrum of Graphene and Graphene Layers. *Phys. Rev. Lett.* **2006**, 97 (18), 187401.
- (17) Castro Neto, A. H.; Guinea, F. Electron-Phonon Coupling and Raman Spectroscopy in Graphene. *Phys. Rev. B: Condens. Matter Mater. Phys.* **2007**, 75 (4), 045404.
- (18) Shi, H.; Poudel, N.; Hou, B.; Shen, L.; Chen, J.; Benderskii, A. V.; Cronin, S. B. Sensing Local Ph and Ion Concentration at Graphene Electrode Surfaces Using *in Situ* Raman Spectroscopy. *Nanoscale* **2018**, 10 (5), 2398–2403.
- (19) Paulus, G. L.; Nelson, J. T.; Lee, K. Y.; Wang, Q. H.; Reuel, N. F.; Grassbaugh, B. R.; Kruss, S.; Landry, M. P.; Kang, J. W.; Vander Ende, E.; Zhang, J.; Mu, B.; Dasari, R. R.; Opel, C. F.; Wittrup, K. D.; Strano, M. S. A Graphene-Based Physiometer Array for the Analysis of Single Biological Cells. *Sci. Rep.* **2015**, 4, 6865.
- (20) Keisham, B.; Cole, A.; Nguyen, P.; Mehta, A.; Berry, V. Cancer Cell Hyperactivity and Membrane Dipolarity Monitoring Via Raman Mapping of Interfaced Graphene: Toward Non-Invasive Cancer Diagnostics. *ACS Appl. Mater. Interfaces* **2016**, 8 (48), 32717–32722.
- (21) Das, A.; Pisana, S.; Chakraborty, B.; Piscanec, S.; Saha, S. K.; Waghmare, U. V.; Novoselov, K. S.; Krishnamurthy, H. R.; Geim, A. K.; Ferrari, A. C.; Sood, A. K. Monitoring Dopants by Raman Scattering in an Electrochemically Top-Gated Graphene Transistor. *Nat. Nanotechnol.* **2008**, 3 (4), 210–5.
- (22) Froehlicher, G.; Berciaud, S. Raman Spectroscopy of Electrochemically Gated Graphene Transistors: Geometrical Capacitance, Electron-Phonon, Electron-Electron, and Electron-Defect Scattering. *Phys. Rev. B: Condens. Matter Mater. Phys.* **2015**, 91 (20), 205413.
- (23) Colherinhas, G.; Fileti, E. E.; Chaban, V. V. The Band Gap of Graphene Is Efficiently Tuned by Monovalent Ions. *J. Phys. Chem. Lett.* **2015**, 6 (2), 302–7.
- (24) Jia, X.; Hu, M.; Soundarapandian, K.; Yu, X.; Liu, Z.; Chen, Z.; Narita, A.; Mullen, K.; Koppens, F. H. L.; Jiang, J.; Tielrooij, K. J.; Bonn, M.; Wang, H. I. Kinetic Ionic Permeation and Interfacial Doping of Supported Graphene. *Nano Lett.* **2019**, 19 (12), 9029–9036.
- (25) Kwon, K. C.; Choi, K. S.; Kim, C.; Kim, S. Y. Role of Metal Cations in Alkali Metal Chloride Doped Graphene. *J. Phys. Chem. C* **2014**, 118 (15), 8187–8193.
- (26) Huang, W.; Wang, G.; Gao, F.; Qiao, Z.; Wang, G.; Chen, M.; Deng, Y.; Tao, L.; Zhao, Y.; Fan, X.; Sun, L. Energy Harvesting from the Mixture of Water and Ethanol Flowing through Three-Dimensional Graphene Foam. *J. Phys. Chem. C* **2014**, 118 (17), 8783–8787.

- (27) Yu, Y.-J.; Zhao, Y.; Ryu, S.; Brus, L. E.; Kim, K. S.; Kim, P. Tuning the Graphene Work Function by Electric Field Effect. *Nano Lett.* **2009**, *9* (10), 3430–3434.
- (28) Morakot, N.; Rakrai, W.; Keawwangchai, S.; Kaewtong, C.; Wannoo, B. Design and Synthesis of Thiourea Based Receptor Containing Naphthalene as Oxalate Selective Sensor. *J. Mol. Model.* **2010**, *16* (1), 129–36.
- (29) Fu, W.; Jiang, L.; van Geest, E. P.; Lima, L. M.; Schneider, G. F. Sensing at the Surface of Graphene Field-Effect Transistors. *Adv. Mater.* **2017**, *29* (6), 1603610.
- (30) Kulkarni, G. S.; Zhong, Z. Detection Beyond the Debye Screening Length in a High-Frequency Nanoelectronic Biosensor. *Nano Lett.* **2012**, *12* (2), 719–723.
- (31) Piccinini, E.; Alberti, S.; Longo, G. S.; Berninger, T.; Breu, J.; Dostalek, J.; Azzaroni, O.; Knoll, W. Pushing the Boundaries of Interfacial Sensitivity in Graphene Fet Sensors: Polyelectrolyte Multilayers Strongly Increase the Debye Screening Length. *J. Phys. Chem. C* **2018**, *122* (18), 10181–10188.
- (32) Xie, Q.; Alibakhshi, M. A.; Jiao, S.; Xu, Z.; Hempel, M.; Kong, J.; Park, H. G.; Duan, C. Fast Water Transport in Graphene Nanofluidic Channels. *Nat. Nanotechnol.* **2018**, *13* (3), 238–245.
- (33) Erickson, D.; Li, D. Microchannel Flow with Patchwise and Periodic Surface Heterogeneity. *Langmuir* **2002**, *18*, 8949–8959.